Supersonic Flow about Ducted Bodies with Subsonic Internal Boundaries

Prakash Bansod*
The City University, London, England

A transient finite-difference method was developed to compute the transonic flow about blunt lipped ducted bodies in supersonic freestreams. A second-order accurate and explicit method was adapted for the computation of the interior regions and a transient method of characteristics was used at the boundaries. The flow velocity at the internal boundary was subsonic; this boundary was specially treated so as to enable the mass flow ratio and/or the axial velocity component to be specified. Three inlet shapes were investigated for axisymmetric and two-dimensional flows: two circular section inlets and an elliptic section.

Nomenclature

a = speed of sound
$ACCT$ = accumulative time, $\Sigma\Delta t$
BOA = radial position of inlet surface, Mesh A
BOB = radial position of inlet surface, Mesh B
C_{DADD} = additive drag coefficient
C_{DEXT} = external drag coefficient
C_{DCOWL} = cowl drag coefficient (obtained by integrating static pressure on the inlet lip)
CPU = central processor unit time (sec)
CFL = Courant-Friedrichs-Lewy stability condition
C_p = pressure coefficient, $(\bar{p}-\bar{p}_\infty)/(\gamma\bar{p}_\infty M_\infty{}^2/2)$
$CONCRIT$ = convergence criterion based on bow shock movement
H = highlight height (Fig. 2)
j = set equal to unity for axisymmetric flow or equal to zero for two-dimensional flow
K_{RUN} = total number of time steps
MOC = method of characteristics
MFR = mass flow ratio
p = pressure normalized with respect to $\bar{p}_\infty$
P = $\log_e(p)$
P_R = total pressure recovery
P_O = total pressure
R = $\log_e(\rho)$
R_H = radius of inlet lip, normalized with respect to H
S = entropy function $(S=P-\gamma R)$
SH = radial position of shock node point
SHX = radial position of axis node point
t = time normalized with respect to $H(\bar{p}_\infty/\bar{p}_\infty)^{1/2}$
t_H = inlet thickness, normalized with respect to H
y = distance measured normal to the axis of symmetry

Velocity Components (normalized with respect to $\bar{a}_\infty/\gamma^{1/2}$)

u, v = radial r and angular θ components
U, V = ξ,η components
W = radial shock velocity

Co-ordinate Directions in the Computational Planes

ZA, YA = Mesh A
ZB, YB = Mesh B

Greek Symbols

$\theta_A, \theta_B, \theta_C$ = angles for the radial lines passing through A, B, and C of Fig. 3.
ρ = density, normalized with respect to $\bar{\rho}_\infty$
λ = fineness ratio
γ = ratio of specific heats
ξ,η = co-ordinate directions used in boundary point evaluation.

Suffixes

$(\,)_\infty$ = freestream conditions
$(\,)_{t_o}$ = t_o plane
$(\,)_N$ = $t_o+\Delta t$ plane
$(\,)_i$ = internal boundary CF
$(\,)_l$ = for $l=1, 2, 3$ refers to quantities evaluated at point G in the t_o plane (Fig. 4).

Superscript

$(\bar{\ })$ = physical variable

I. Introduction

In recent years there has been a resurgence of interest in transonic aircraft. In the United States, this interest has been encouraged in the case of commercial aircraft by the environmentalist lobby regarding the sonic boom created by supersonic transports. It is known that aircraft flying in the stratosphere up to Mach numbers of 1.2 do not usually create a sonic boom at sea level. Williams,[1] Pearcey,[2] and Goodmanson[3] published papers which were devoted to the preliminary design study of the next generation of transonic transports. These papers evaluate the technical feasibility of the next generation of aircraft flying in the Mach number range $0.9 \leq M_\infty \leq 1.2$. At slightly higher Mach numbers in the range $1.4 \leq M_\infty \leq 1.6$, consideration is also being given to asymmetric wing configurations pioneered by Jones.[5] Aircraft designed to cruise at $M_\infty < 1.5$ could use Pitot air-intakes because the total pressure recovery P_r is approximately equal to that occurring through a normal shock at the same M_∞ (see Ref. 4) and is within acceptable limits. Aircraft cruising in the Mach number range $2.0 \leq M_\infty \leq 3.0$, normally use additional compression surfaces such as centerbodies and movable ramps to enhance their pressure recovery performance. Due to local separation effects on sharp inlets at subsonic Mach numbers, most inlets are usually blunted to improve their subsonic performance.

Presented as Paper 74-18 at the AIAA 12th Aerospace Sciences Meeting, Washington, D.C., January 30-February 1, 1974; submitted February 15, 1974; revision received November 11, 1974. The financial support for this research was obtained initially through a City University Research Studentship and later continued under a United Kingdom Ministry of Defence Contract (Agreement No. AT/2090/029).

Index categories: Subsonic and Transonic Flow; Airbreathing Propulsion, Subsonic and Supersonic.

*Formerly Research Assistant, Department of Aeronautics; now Aerodynamicist, British Aircraft Corporation, Weybridge, U.K.

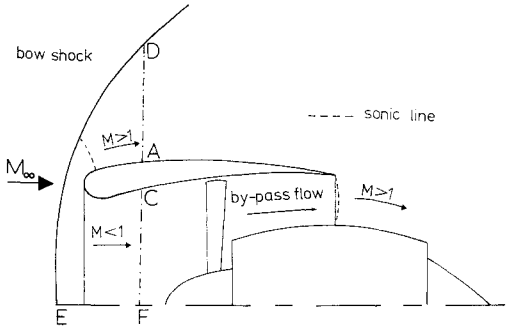

Fig. 1 High bypass ratio engine.

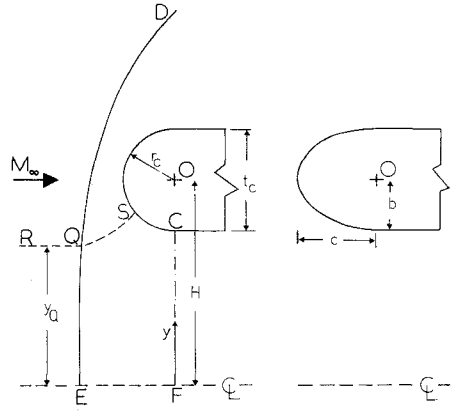

Fig. 2 Inlet lip notation.

This paper concerns the prediction of the flow about two-dimensional and axisymmetric blunt lipped air inlets in supersonic freestreams: essentially ducted bodies. The contribution made here is the presentation of a numerical scheme which enables the internal flow to remain subsonic for a specified mass flow ratio (*MFR*) and/or axial velocity component. Figure 1 shows a sketch of a high bypass ratio engine immersed in a supersonic airstream. The problem is to predict the flow about a region of this configuration bounded by the bow shock *DE* and the cowl lip. The computation is terminated at a convenient subsonic boundary *CF* internally and a supersonic boundary *AD* externally. The regions downstream of the boundaries *AD* and *CF* are not computed in this paper. The supersonic flow downstream of *AD* can be computed using the method of characteristics[6] or a shock-capturing finite-difference method.[7]

The flow upstream of the bow shock is assumed to be uniform; i.e., the effects of center bodies or compression ramps are neglected. However, "two-dimensional" fuselage inlets are within the scope of this work. The gas flow (air) is taken to be ideal, inviscid and adiabatic with a specific heat ratio of 1.4. Figure 2 illustrates the two types of inlet shapes considered. Inlets A and B have circular sections. Inlet C has an elliptic section.

The inlet radius is nondimensionalized as $R_H = r_c/H$ and the inlet thickness $t_H = t_c/H$. The fineness ratio $\lambda = (c/b)$. With reference to Fig. 2, the mass flow ratio can be defined as

$$MFR = \int_F^C (\bar{v}/\bar{U}_\infty)(\bar{\rho}_i/\rho_\infty)(2y)^j dy/(H)^{1+j} \qquad (1)$$

Table 1 Inlet geometry

Inlet	A	B	C
R_H	0.35	0.25	...
t_H	0.70	0.50	0.50
λ	1.00	1.00	1.50

where $\bar{U}_\infty$ is the freestream velocity and y is the distance measured from the axis. Alternatively,

$$MFR = (y_Q/H)^{1+j} \qquad (2)$$

where $j=0$ for two-dimensional flow and $j=1$ for axisymmetric flow. The highlight height H is set equal to unity and defines a length scale for the computations.

II. Selection of a Numerical Method

The flow about the blunt lipped inlet shown in Fig. 1 is transonic. A detached shock wave occurs in front of the inlet with the internal flow through boundary *CF* remaining subsonic, while the external flow accelerates to supersonic velocities. A sonic line spans the region between the inlet lip and the bow shock. The nature of the flow is similar to that occurring in the well-known problem of a blunt body immersed in a supersonic stream. For steady state conditions, the nonlinear partial differential equations describing the flow are elliptic in the subsonic regions and hyperbolic in the supersonic regions. This nonhomogeneity in the type of partial differential equations is the cause of the major difficulties associated with transonic flow problems.

Dorodnitsyn[8] presented a method of solving the conservation form of the equations of motion, called the Method of Direct Integrals. The physical region is divided into one or more strips and the equations are integrated to the boundaries of each strip. The convergence of the method can only be checked by increasing the number of strips which in turn increases the complexity of the solution.

The Relaxation Method which is used to solve the transonic small perturbation potential equation has proved to be an economic method of solving supercritical flow problems. Bailey[9] used this method to compute flows with detached shock waves. Because of the assumption of isentropic flow, this method can only be used for $M_\infty < 1.2$.

The approach to most steady state transonic flow problems is simplified by considering the fluid motion to be variant with time. The unsteady equations of motion are solved numerically and the steady state is reached asymptotically in time. The advantage of the Time-Dependent or Transient Numerical Method is that the unsteady equations of motion (for inviscid flow) are hyperbolic throughout the region of interest. Hence the transient method of characteristics (MOC) or a transient finite difference method can be used to solve them.

The literature on this subject shows several successful applications to the blunt body problem[10-12] using transient finite difference methods. This prompted the selection of the transient finite difference method for the present problem; also it is conceptionally simple due to the explicit nature of the solution. Starting from any realistic initial conditions the convergence to a unique solution could be checked by merely reducing the size of the finite difference mesh.

D'Souza[13] made a major contribution to the ducted body problem by computing the hypersonic flow about blunt lipped ducted bodies using Moretti's[10] scheme for interior and boundary points. The flow at the interior boundary was supersonic. Garner[14] computed the flow about inlets with centerbodies using the Godunov[12] scheme. A sharp lipped inlet was considered at $M_\infty = 2.0$. However, these results required more computer time than D'Souza's and also appeared to be less accurate when compared with experimental results due to the first-order accuracy of the Godunov scheme.

III. Application of the Transient Finite Difference Method

We now proceed to describe the computational procedures used to obtain the flowfield about ducted bodies with subsonic internal boundaries.

Computation of Interior Points

Referring to Fig. 3, the governing equations of motion can be written in terms of polar (two-dimensional) or toroidal (axisymmetric) coordinates with the origin at 0.

Continuity Equation

$$\frac{\partial R}{\partial t}+\frac{\partial u}{\partial r}+u\frac{\partial R}{\partial r}+\frac{u}{r}+\frac{1\partial v}{r\,\partial\theta}+\frac{v\,\partial R}{r\,\partial\theta}$$

$$+j(u\sin\theta+v\cos\theta)/(H+r\sin\theta)=0 \tag{3}$$

Momentum Equations

$$\frac{\partial u}{\partial t}+u\frac{\partial u}{\partial r}+\frac{v\,\partial u}{r\,\partial\theta}-\frac{v^2}{r}+\frac{p\,\partial P}{\rho\,\partial r}=0 \tag{4}$$

$$\frac{\partial u}{\partial t}+u\frac{\partial v}{\partial r}+\frac{v\,\partial v}{r\,\partial\theta}+\frac{uv}{r}+\frac{1}{r}\frac{p\,\partial P}{\rho\,\partial\theta}=0 \tag{5}$$

Conservation of Entropy along a Particle Path

$$\frac{\partial S}{\partial t}+u\frac{\partial S}{\partial r}+\frac{v\,\partial S}{r\,\partial\theta}=0 \tag{6}$$

Equations (3-6) are solved using a scheme originally reported by Moretti[10] which is based on a second-order accurate Taylor series expansion. The density function R for example, can be evaluated as follows:

$$R(t_0+\Delta t)=R(t_0)+\left(\frac{\partial R}{\partial t}\right)\Delta t+\left(\frac{\partial^2 R}{\partial t^2}\right)\frac{\Delta t^2}{2} \tag{7}$$

The time derivatives in Eq. (7) are eliminated in terms of spatial derivatives using Eqs. (3-6). A similar procedure is followed for $u(t_0+\Delta t)$, $v(t_0+\Delta t)$ and $S(t_0+\Delta t)$. The spatial derivatives are evaluated using central differences in a finite difference grid. The time step size Δt is governed by a stability condition similar to the Courant-Friedrichs-Lewy condition.[16]

In practice, the physical plane is transformed into two rectangular computational grids (Fig. 3), designated Mesh A and Mesh B. Equations (3-6) are rewritten[13,15] in terms of these computational coordinates before they are solved by the preceding scheme. In order to evaluate interior points on the intermesh boundary BE, extra rows of points B′E′ and B″E″ for each mesh are used.

Computation of Boundary Points

The *MOC* is used to evaluate the boundary points along with some auxiliary conditions depending on the nature of the boundary. In Fig. 4, PQR is any arbitrary boundary. Using $\xi-\eta$ co-ordinates the equations of motion can be expressed as follows:

$$\frac{\partial P}{\partial t}+U\frac{\partial P}{\partial\xi}+\gamma\frac{\partial U}{\partial\xi}+\gamma\frac{\partial V}{\partial\eta}+V\frac{\partial P}{\partial\eta}+j\gamma V_c/y=0 \tag{8}$$

$$\frac{\partial U}{\partial t}+U\frac{\partial U}{\partial\xi}+\frac{a^2}{\gamma}\frac{\partial P}{\partial\xi}+V\frac{\partial U}{\partial\eta}=0 \tag{9}$$

$$\frac{\partial V}{\partial t}+U\frac{\partial V}{\partial\xi}+V\frac{\partial V}{\partial\eta}+\frac{a^2}{\gamma}\frac{\partial P}{\partial\eta}=0 \tag{10}$$

where V_c is the velocity component normal to the axis of symmetry.

The computational effort and complexity associated with *MOC* in three independent variables is well-known.[17] To simplify the calculation of each boundary point, Moretti[18] proposed that by a judicious orientation of the $\xi-\eta$ coordinate system (see Fig. 5), the derivatives of the dependent variable with respect to η can be assumed to be independent of

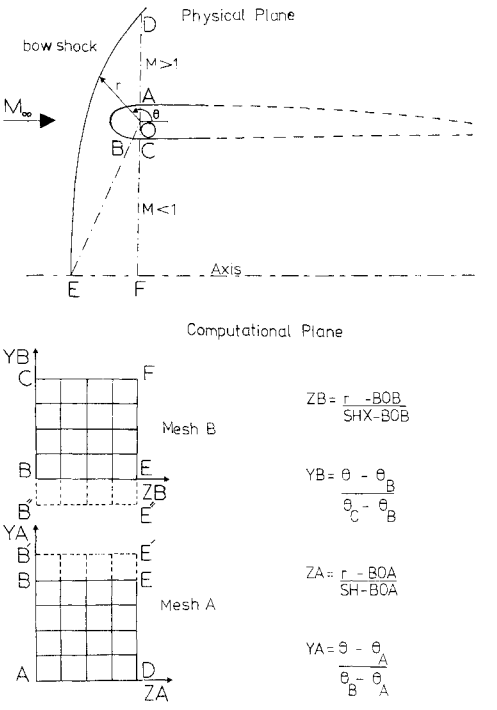

Fig. 3 Physical and computational planes.

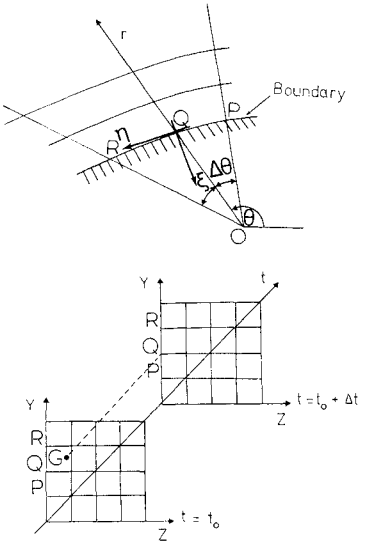

Fig. 4 Evaluation of boundary points.

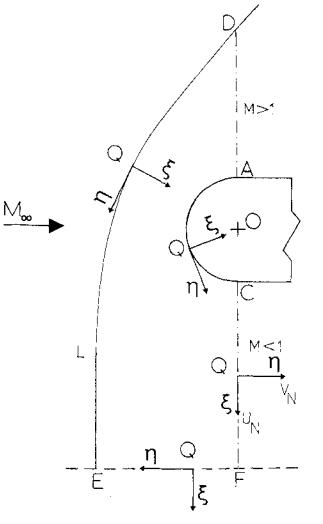

Fig. 5 ξ,η coordinates.

time t. This gives a set of quasi-linear hyperbolic equations in two independent variables (ξ, t). The characteristic and corresponding compatibility equations are given by (see Appendix)

$$d\xi/dt = U + a \tag{11}$$

along which

$$\frac{dP}{dt} + \gamma \frac{dU}{dt} = -\left(\gamma \frac{\partial V}{\partial \eta} + V \frac{\partial P}{\partial \eta} + \frac{V\gamma}{a} \frac{\partial U}{\partial \eta} + j\gamma V_c/y\right)_{t_0} = \text{RHS1} \tag{12}$$

holds; and

$$d\xi/dt = U - a \tag{13}$$

along which

$$\frac{dP}{dt} - \frac{\gamma}{a} \frac{dU}{dt} = -\left(\gamma \frac{\partial v}{\partial \eta} + V \frac{\partial P}{\partial \eta} - \frac{V\gamma}{a} \frac{\partial U}{\partial \eta} + j\gamma V_c/y\right)_{t_0} = \text{RHS2} \tag{14}$$

holds. Along a particle path,

$$d\xi/dt = U \tag{15}$$

$$dS/dt = -(V \partial S/\partial \eta)_{t_0} \tag{16}$$

holds. Integrating Eqs. (12, 14, and 16) gives

$$P_N + \frac{\gamma}{\bar{a}_1} U_N = P_1 + \frac{\gamma}{\bar{a}_1} U_1 + (\text{RHSI})\Delta t \tag{17}$$

$$P_N - \frac{\gamma}{\bar{a}_2} U_N = P_2 - \frac{\gamma}{\bar{a}_2} U_2 + (\text{RHS2})\Delta t \tag{18}$$

$$S_N = S_3 - \left(V \frac{\partial S}{\partial \eta}\right)_{t_0} \Delta t \tag{19}$$

where $\bar{a}_i = (a_i + a_N)/2$ for $1 = 1, 2$.

The origin of the $\xi - \eta$ coordinate system in Fig. 4 is situated at point Q in the $t_o + \Delta t$ plane. The right-hand sides of Eqs. (17-19) are evaluated by integrating Eqs. (11, 13, and 15) respectively, so as to locate the coordinates of the disturbance which starts from point G in the initial time plane t_o and reaches Q at $t_o + \Delta t$. Improved results are obtained by allowing a translation in the η direction governed by the equation,

$$d\eta/dt = V \tag{20}$$

when locating the coordinates of G in the t_o plane. The right-hand sides of Eqs. (17-19) are then evaluated at point $G_l (l = 1, 2, 3)$ using an interpolation procedure. For each boundary point the MOC involves an iterative process because the slope of the characteristic is initially an approximate one. Improved values of these slopes are obtained through a Newton-Raphson process.

The pressure P_N on the inlet surface and axis of symmetry was evaluated using Eqs. (11, 17, and 20) and Eqs. (13, 18, and 20), respectively. The boundary condition at both boundaries was $U_N = 0$. The tangential velocity component V_N was evaluated by applying the MacCormack scheme[19] to Eq. (10).

The entropy S_N on the inlet surface can be calculated using two methods. Method 1 involves setting S_N equal to the value obtained if the stagnation streamline passed through a normal shock for the given M_∞. Method 2 involves calculating the point of intersection between the stagnation streamline R Q S and the bow shock D E in Fig. 2. y_Q can be calculated from Eq. (2) as the *MFR* is known or can be evaluated at boundary C F. The entropy at point Q is then evaluated using the inclined shock relations. The entropy at the stagnation point on the inlet surface is then set equal to the value at point Q. For other points on the inlet surface the entropy is obtained by tracing the particle path. Initial checks showed that the differences in the converged values of S_N obtained using methods 1 and 2 were negligible. Hence for simplicity method 1 was used. As the axis of symmetry is also a particle path, S_N was obtained by a similar process. Knowing S_N and P_N, R_N is given by

$$S_N = P_N - \gamma R_N \tag{21}$$

The bow shock DE of Fig. 5 is treated as a moving discontinuity across which the Rankine-Hugoniot relations hold. Equations (13, 18, and 20) are used at Q to obtain U_N. P_N and U_N are also evaluated using the Rankine-Hugoniot relations and this value of U_N is compared with that obtained from Eq. (18). The difference between these two values of U_N is used in the Newton-Raphson process so as to obtain a better estimate of the radial shock velocity W. The radial position of the shock wave node point is given by

$$SH(t_0 + \Delta t) = SH(t_0) + W\Delta t \tag{22}$$

Subsonic Internal Boundary

It would be convenient to treat boundary CF in Fig. 5 as a specified boundary such that *MFR* would be set a priori by a particular choice of P, R, U and V at *CF* and held constant throughout the computation. Unfortunately, specified subsonic boundaries in a transient computational procedure are not conducive to a stable computation. When disturbances from the interior points reach the subsonic boundary, they are reflected back into the computed region if values are held constant. This is because there is no mechanism for absorbing the disturbances. Sharp peaks in the distribution of the dependent variables occur and the computation soon becomes unstable.

The approach adopted here is to calculate U_N and P_N by solving Eqs. (17) and (18) simultaneously and S_N from Eq. (19). V_N is then calculated using the integral expression for the *MFR*, Eq. (1) (with $H = 1$),

$$V_N = (MFR\gamma^{1/2} M_\infty)/\int_F^C e^{R_N} (2y)^j dy \tag{23}$$

as

$$R_N = \log_e [\bar{\rho}(t_0 + \Delta t)/\bar{\rho}_\infty]$$

It was assumed that V_N was constant along the boundary CF but varied from one time step to another, constrained by the specified *MFR*. Due to stability problems Eq. (23) was not used for axisymmetric flows; instead V_N was set equal to a constant based on the one-dimensional area-Mach number relationship for isentropic flow.

The manner in which the flow variables are calculated at the subsonic boundary does not take into account the influence of the inlet gometry downstream of CF. Although the condition of uniformity in axial velocity at CF does not cause a serious loss of generality, it is best suited for inlets with constant internal diameter downstream of CF.

Summary

The computations start from rough initial conditions which are estimated from previous calculations and/or empirical methods. A stable time step is computed followed by com-

putational procedures for the interior and boundary points. New values are reset so as to become initial conditions for the next time step. This process is repeated until the results are observed to converge asymptotically in time. The movement of the bow shock was found to be a good measure of convergence. A convergence criterion, *CONCRIT*, can be defined as the average value of $|W \cdot \Delta t|$ for all the shock points. It was found that values of *CONCRIT* $<5\times10^{-5}$ were usually sufficient to ensure convergence.

IV. Discussion of Results

Axisymmetric Flow

Initially the flow about Inlet B at $M_\infty = 2.81$ was calculated. The effect of mesh size for the same $MFR = 0.59$ was studied. The two node densities for the coarse and fine mesh sizes were 5×10 (Mesh A), 5×4 (Mesh B) and 10×20 (Mesh A), 10×8 (Mesh B), respectively. Figure 6 compares Mach number and pressure distribution on the inlet surface for the two node densities. Reducing the mesh size improves the pressure results in the region of the stagnation point for a value of θ corresponding to $M=0$.

Figure 7 shows the transient behavior of the normal pressure drag coefficient C_{DCOWL} and the pressure recovery P_R. A common feature of the curves in Fig. 7 is that the fluctuations reduce as convergence is reached. For the same initial conditions and boundary conditions such as inlet shape, M_∞ and *MFR* , the value of t for which convergence occurs is almost independent of node density. However, the number of time steps required for the coarse mesh were 750 and 1500 for fine mesh. The broken line in Fig. 7b indicates the value of P_R obtained if internal mass flow passed through a normal shock. The coarse mesh values lie below those of the more accurate fine mesh and normal shock values. This is indicative of the effective increase in entropy (or lowering of P_O) due to the dissipative nature of the difference scheme. This effect is accentuated with a coarse mesh which has larger truncation errors.

Figure 8 shows a flow direction plot for Inlet C at $M_\infty = 2.81$. The conjectured position of the stagnation streamline (shown by a broken line) is drawn by studying the local streamline pattern. The distance y_Q agrees with that obtained by using Eq. (2) for the given *MFR* of 0.59. This agreement provides an independent check on the consistency of the numerical computation specially with regard to the manner in which the boundary CF is treated.

An attempt was made to produce numerical results for a circular lipped inlet with $R_H = 0.0935$ so that a comparison with experiment could be made. Large negative shock velocities were observed in the region between point L and point E in Fig. 5. The results soon became unstable. These instabilities appear to have been caused by the limitations of the one-dimensional unsteady *MOC* used at the shock and subsonic boundary points. These problems appear to have been remedied by smoothing the dependent variables at Mesh B (which is adjacent to the subsonic boundary CF) at every 25 time steps. These results are presented in Fig. 9 for 6000 time

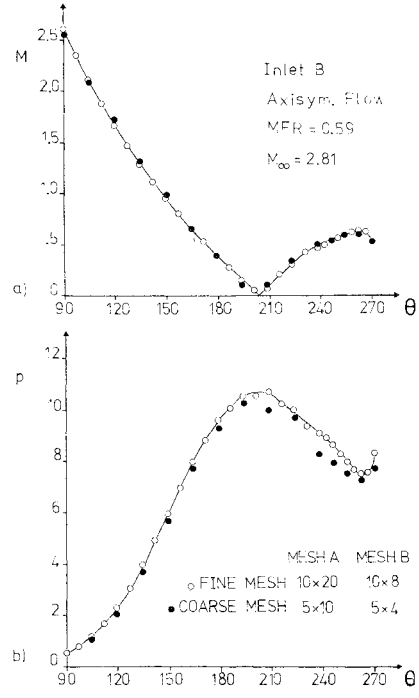

Fig. 6 Pressure and Mach number distribution. a) Mach number; b) pressure.

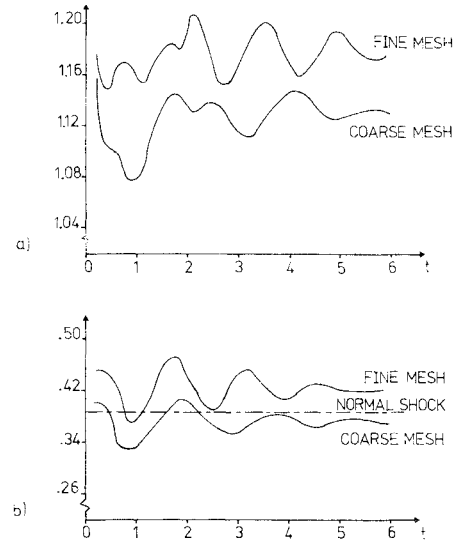

Fig. 7 Transient behavior of C_{DCOWL} and P_r. a) C_{DCOWL}; b) P_R.

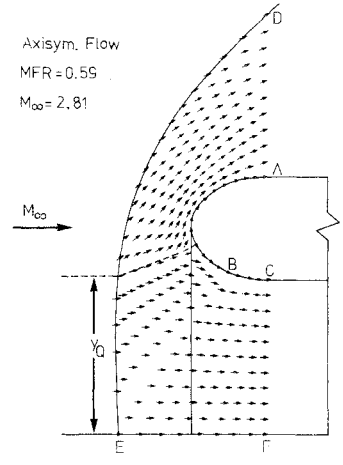

Fig. 8 Flow direction plot about Inlet C.

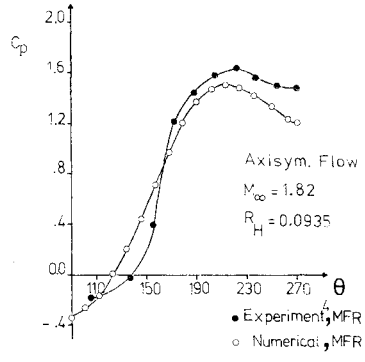

Fig. 9 Numerical and experimental results.

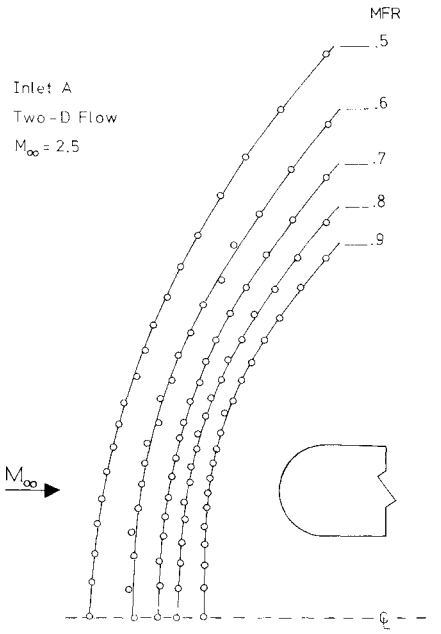

Fig. 10 Variation of bow shock position with *MFR*.

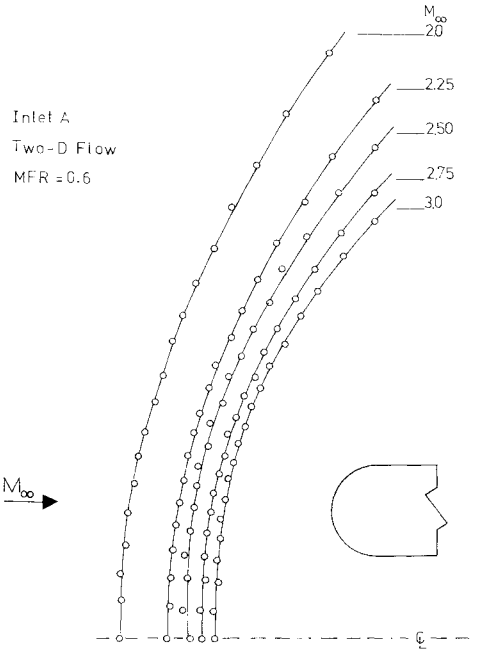

Fig. 11 Variation of bow shock position with M_∞.

steps. The stagnation value of C_p is under-stimated by 8% relative to the experimental values at $M_\infty = 1.82$. Hence this method is not sufficiently accurate to determine the pressure distribution on thin cowls. However, the scheme could be used to predict the bow shock geometry. The smoothing process prevents numerical instability but also affects the accuracy of the results. Reducing the mesh size would not improve the accuracy in this case, due to the inherent limitations of the unsteady one-dimensional boundary evaluation method. Inlet lips with $t_H \geq 0.5$ (or $R_H \geq 0.25$ for circular lip sections) did not require any smoothing.

Two-Dimensional Flow

Two dimensional computations were made for Inlet A in the freestream Mach number range $2 \leq M_\infty \leq 3$ at a constant *MFR* of 0.6. At $M_\infty = 2.5$, results were also produced for different mass flow ratios in the range $0.5 \leq MFR \leq 0.9$. Figure 10 shows the variation of bow shock position and shape with *MFR* at $M_\infty = 2.5$. As the *MFR* is increased, the bow shock detachment distance reduces. Alternatively, Fig. 11 shows a reduction in the shock detachment distance when M_∞ increased at a constant value of $MFR = 0.6$. This trend is similar to the reduction of shock detachment distance for a blunt body in a supersonic stream of increasing M_∞.

Figure 12 shows the variation of Mach number and static pressure C_p on the surface of Inlet A for $MFR = 0.5$, 0.7, and 0.9 at $M_\infty = 2.5$. In Fig. 12, the stagnation point which occurs at $M = 0$, moves away from the leading edge (which is at $\theta = 180°$) towards C as the *MFR* is reduced.

At $M_\infty = 2.5$ and $MFR = 0.6$, the inlet drag coefficients for Inlet A and symmetric ellipse sectioned Inlets (with different γ) were calculated and presented in Fig. 13. Figure 13a shows the variation of C_D with *MFR* at $M_\infty = 2.5$. There is an expected reduction of C_{DADD} with an increase of *MFR*. This is because at high values of *MFR* the shock detachment distance is reduced and hence the length of the stagnation streamline QS (Fig. 2) reduces; consequently there is also a reduction in C_{DEXT}.

Figure 13b shows the variation of C_D with fineness ratio λ.

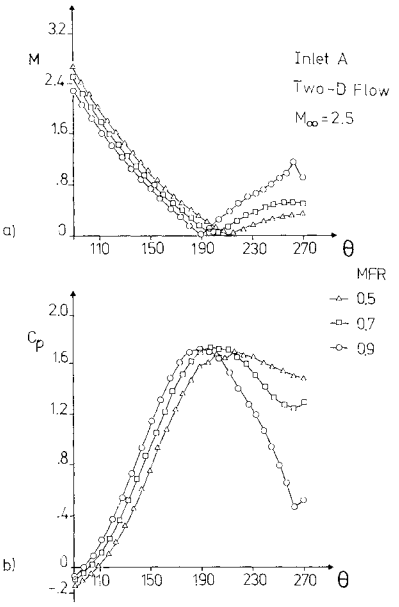

Fig. 12 Variation of M and C_p with *MFR*. a) M; b) C_p.

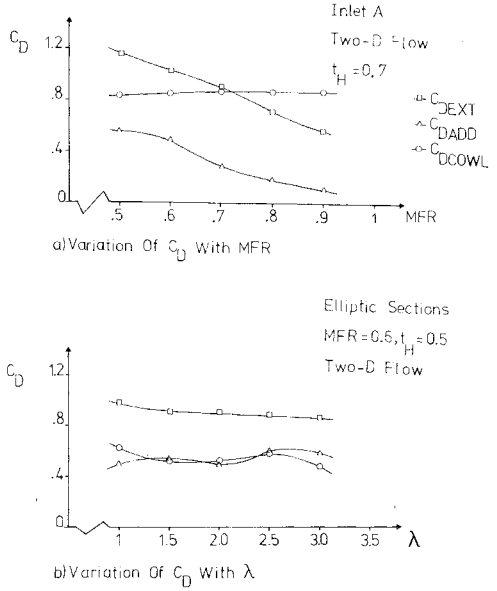

Fig. 13 C_D results for $M_\infty = 2.5$.

Table 2 Typical computation time for some case studies

M_∞	Inlet shape	Node density	*MFR*	K_{RUN}	*ACCT*	*CONCRIT* (x 10^{-5})	CPU CDC 7600
2.25	A (2-D)	10 × 18 10 × 9	0.6	2000	14.19	6.5	239
2.75	A (2-D)	10 x 18 10 × 8	0.6	2000	13.12	4.93	226
2.81	B (AXSY)	10 × 20 10 × 8	0.59	1500	5.88	2.4	198
2.81	B (AXSY)	5 × 10 5 × 4	0.59	750	6.00	2.9	116

The inlets used had a thickness parameter of $t_H = 0.5$. There appears to be a reduction of C_{DEXT} with an increase in fineness ratio. The external drag is effectively the resultant drag acting on the inlet. The behavior of C_{DEXT} is comparable to the behavior of C_D obtained for blunt bodies which usually show a reduction in C_D with an increase of λ for a given M_∞.

Table 2 gives some examples of Central Processor Unit time (in seconds) required using a CDC7600 computer for some typical case studies. The lip radius size governed the size of the time step size Δt through the *CFL* condition. Hence, small inlet lips required larger amounts of CPU time. The CPU time was also observed to increase with a reduction in M_∞ for the same inlet geometry and node density.

V. Conclusions

The transonic flow about blunt lipped inlets was calculated using a transient finite difference method. The main contribution is the treatment of the subsonic internal boundary which enabled the *MFR* and/or the axial velocity to be specified as a boundary condition. Converged results were obtained for inlet lips with a thickness parameter of $t_H \geq 0.5$ and fineness ratio $\lambda \leq 3$. For inlets with $t_H \leq 0.5$, a smoothing routine was used to obtain stable results. The variation of the bow shock position with M_∞ and *MFR* and the observed position of the intersection of the stagnation streamline with the bow shock at a given *MFR*, showed that the numerical method used interpreted the physical situation correctly.

The boundary evaluation method used here does not give accurate results for pressure distributions on thin inlet sections. An improvement in the results, for thin inlet sections and lower supersonic freestream Mach numbers, could be achieved by a further development of the present scheme for the boundary points as outlined by Butler.[17]

Appendix: Derivation of Characteristic Equations and Compatability Equations for the Evaluation of Boundary Points

To avoid the complexities associated with the *MOC* for three independent variables, the derivatives with respect to η were assumed to be independent of time t. This appears to be a plausible assumption if the η axis at a boundary point is approximately in the predominent direction of the local flow. Thus the derivatives $\partial P/\partial\eta$, $\partial v/\partial\eta$ and $\partial u/\partial\eta$ in Eqs. (8-10) can be taken over to the right hand side and treated as constant terms. This gives a set of partial differential equations with two independent variables ξ and t which can be expressed as follows:

$$\frac{\partial P}{\partial t} + U\frac{\partial P}{\partial \xi} + \gamma\frac{\partial U}{\partial \xi} = -\left(\gamma\frac{\partial V}{\partial \eta} + j\frac{\gamma V_c}{y} + V\frac{\partial P}{\partial \eta}\right) = b_1 \tag{A1}$$

$$\frac{\partial U}{\partial t} + U\frac{\partial U}{\partial \xi} + \frac{a^2}{\gamma}\frac{\partial P}{\partial \xi} = -\left(V\frac{\partial U}{\partial \eta}\right) = b_2 \tag{A2}$$

$$\frac{\partial V}{\partial t} + U\frac{\partial V}{\partial \xi} = -\left(V\frac{\partial V}{\partial \eta} + \frac{a^2}{\gamma}\frac{\partial P}{\partial \eta}\right) = b_3 \tag{A3}$$

Characteristic Equations

Consider the transformation to the following co-ordinate system, $\alpha = \alpha(\xi, t)$. The preceding equations can then be expressed as follows:

$$\begin{bmatrix} (\partial\alpha/\partial t + U\,\partial\alpha/\partial\xi) & \gamma\,\partial\alpha/\partial\xi & — \\ a^2/\gamma(\partial\alpha/\partial\xi) & (\partial\alpha/\partial t + U\,\partial\alpha/\partial\xi) & — \\ — & — & (\partial\alpha/\partial t + U\,\partial\alpha/\partial\xi) \end{bmatrix} \begin{bmatrix} \partial P/\partial\alpha \\ \partial U/\partial\alpha \\ \partial V/\partial\alpha \end{bmatrix} = \begin{bmatrix} b_1 \\ b_2 \\ b_3 \end{bmatrix} \tag{A4}$$

Characteristic surfaces are defined as surfaces across which derivatives of the dependent variables are discontinuous. If $\alpha_1 = \text{constant}$ is such a surface, the derivatives $\partial P/\partial\alpha$, $\partial U/\partial\alpha_1$, and $\partial V/\partial\alpha_1$ would be indeterminate on it. This condition could be alternatively expressed by,

$$\begin{vmatrix} (\partial\alpha_1/\partial t + U\,\partial\alpha_1/\partial\xi) & \gamma\,\partial\alpha_1/\partial\xi & — \\ a^2/\gamma(\partial\alpha_1/\partial\xi) & (\partial\alpha_1/\partial t + U\,\partial\alpha_1/\partial\xi) & — \\ — & — & (\partial\alpha_1/\partial t + U\,\partial\alpha_1/\partial\xi) \end{vmatrix} = 0$$

Hence the characteristic curves are given by,

$$(\partial\alpha_1/\partial t + U\,\partial\alpha_1/\partial\xi) = 0 \tag{A5}$$

and

$$(\partial\alpha_1/\partial t + U\,\partial\alpha_1/\partial\xi)^2 - a^2(\partial\alpha_1/\partial\xi)^2 = 0 \tag{A6}$$

If $\alpha_1 = \alpha_1(\xi,t)$ then

$$d\xi/dt = -(\partial\alpha_1/\partial t)/(\partial\alpha_1/\partial\xi).$$

Hence from (A5) and (A6),

$$d\xi/dt = U \tag{A7}$$

which is a particle path and the two wave fronts are given by

$$d\xi/dt = U \pm a \tag{A8}$$

Compatibility Equations

The variation of U and P along characteristic lines in the ξ,t plane can be expressed as

$$dU/dt = \partial U/\partial t + (\partial U/\partial\xi)(d\xi/dt) \tag{A9}$$

and

$$\frac{dP}{dt} = \frac{\partial P}{\partial t} + \frac{\partial P}{\partial\xi}\frac{d\xi}{dt} \tag{A10}$$

Equation (A2) can be rewritten as follows:

$$\frac{\partial U}{\partial t} + (U+a)\frac{\partial U}{\partial\xi} + \frac{a^2}{\gamma}\frac{\partial P}{\partial\xi} - a\frac{\partial U}{\partial\xi} = b_2$$

using (A9) with $d\xi/dt = U + a$, this can be written as

$$\frac{dU}{dt} + \frac{a^2}{\gamma}\frac{\partial P}{\partial\xi} - a\frac{\partial U}{\partial\xi} = b_2 \tag{A11}$$

Similarly, (A1) can be rewritten using (A10)

$$\frac{dP}{dt} + \gamma\frac{\partial U}{\partial\xi} - a\frac{\partial P}{\partial\xi} = b_1 \tag{A12}$$

Hence (A11) and (A12) combined to give the compatibility equation for the $d\xi/dt = U + a$ characteristic,

$$\frac{dP}{dt} + \frac{\gamma}{a}\frac{dU}{dt} = -\left(\frac{V\gamma}{a}\frac{\partial U}{\partial\eta} + \frac{\gamma\,\partial V}{\partial\eta} + V\frac{\partial P}{\partial\eta} + j\gamma V_c/y\right) \tag{A13}$$

Similarly for the $d\xi/dt = U - a$ characteristic

$$\frac{dP}{dt} - \frac{\gamma}{a}\frac{dU}{dt} = -\left(-\frac{V\gamma}{a}\frac{\partial U}{\partial\eta} + \gamma\frac{\partial V}{\partial\eta} + V\frac{\partial P}{\partial\eta} + j\gamma V_c/y\right) \tag{A14}$$

Finally, along the particle path $d\xi/dt = U$,

$$dS/dt = \partial S/\partial t + U\partial S/\partial\xi = -(V\,\partial S/\partial\eta) \tag{A15}$$

References

[1] Williams, L.J., "Transonic Transports Study-Summary," TM-X62156 May, 1972, NASA.

[2] Pearcey, H. H. and Osborne, J., "Some Problems and Features of Transonic Aerodynamics," ICAS Paper 70-14, Rome, 1970.

[3] Goodmanson, L.T., "Transonic Transports," *Astronautics and Aeronautics,* Vol. 9, Nov. 1971, pp. 46-57.

[4] Gibbings, J.C., "Pressure Measurements on Three Nose Air Intakes at Transonic and Supersonic Speeds with an Analysis of their Drag Characteristics," Rept. Aero 2637, 1960, Royal Aircraft Establishment, Farnborough, England.

[5] Jones, R.T., "New Design Goals and a New Shape for the SST," *Astronautics and Aeronautics,* Vol. 10, Dec. 1972, pp. 66-70.

[6] Gee, K.C.E., "Two-Dimensional and Axisymmetric Ideal Gas Flow by the Method of Characteristics," *A Catalogue of Digital Computer Programs in Fluid Dynamics,* (Procurement Executive) Rept. BR29590, Sept. 1972, Ministry of Defence, London.

[7] Kutler, P. and Lomax, H., "A Systematic Development of the Supersonic Flow Fields over and behind Wing and Wing-Body Configurations using a Shock-Capturing Finite-Difference Approach," AIAA Paper 71-99, New York, Jan. 1971.

[8] Dorodnitsyn, A.A., "A Contribution to the Solution of Mixed Problems of Transonic Aerodynamics," *Advanced in Aeronautical Sciences,* Vol. 2, Pergamon, New York, 1959, pp. 832-843.

[9] Bailey, F.R., "Numerical Calculations of Transonic Flow about Slender Bodies of Revolution," TND-6582, 1971, NASA.

[10] Moretti, G. and Abbett, M., "A Time Dependent Computation for Blunt Body Flows," *AIAA Journal,* Vol. 4, Dec. 1966, pp. 2136-2141.

[11] Barnwell, R.W., "A Time Dependent Method for Calculating Supersonic Blunt-Body Flow Fields with Sharp Corners and Embedded Shock Waves," TND-6031, 1970, NASA.

[12] Godunov, S.K., Zabrodin, A.V., and Prokopov, G.P., "A Computational Scheme for Two-Dimensional Non-Stationary Problems of Gas Dynamics and Calculations of the Flow for a Shock Wave approaching a Stationary State," *USSR Journal of Computation and Mathematical Physics,* 1962, pp. 1187-1219.

[13] D'Souza, N., Molder, S., and Moretti, G., "A Time Dependent Method for Blunt Leading Edge Hypersonic Internal Flow," *AIAA Journal,* Vol. 10, May 1972, pp. 617-622.

[14] Garner, J.E., "Inlet Flow Field Analysis using the Godunov Differencing Scheme," Ph.D. thesis, 1972, University of Tennessee, Knoxville, Tenn.

[15] Bansod, P., "A Transient Numerical Method for Computing the Flow about Ducted Bodies in Supersonic Freestreams," Ph.D. thesis, 1973, The City University, London.

[16] Courant, R., Friedrichs, K., and Lewy, H., "On the Partial Differential Equations of Mathematical Physics," *IBM Journal of Research and Development,* Vol. 11, 1967.

[17] Butler, D.S., "The Numerical Solution of Partial Differential Equations in Three Independent Variables," *Proceedings of the Royal Society, (London),* Series A, Vol. 255, 1960.

[18] Moretti, G., "Three-Dimensional Supersonic Flow Computations," *AIAA Journal,* Vol. 1, Sept. 1963, pp. 2192-2193.

[19] MacCormack, R.W., "The Effect of Viscosity on Hypervelocity Impact Cratering," AIAA Paper 69-354, Cincinnati, Ohio, April 1969.